Perinone Isomerism Effect on Proton Insertion Chemistry

Qing Lang, Jian Zhang, Ziqi Tian, Qi Fan, Kun Liang, Yunan Wang, Evgenia Dmitrieva, Liang Chen, Congxue Liu, Mingchao Wang*, Maryam AlNahyan, Panče Naumov*, and Gang Wang*

Experimental Section

All solvents, reagents and chemicals were purchased from commercial suppliers, such as Sigma-Aldrich, Aladdin, and used without further purification unless specially addressed.

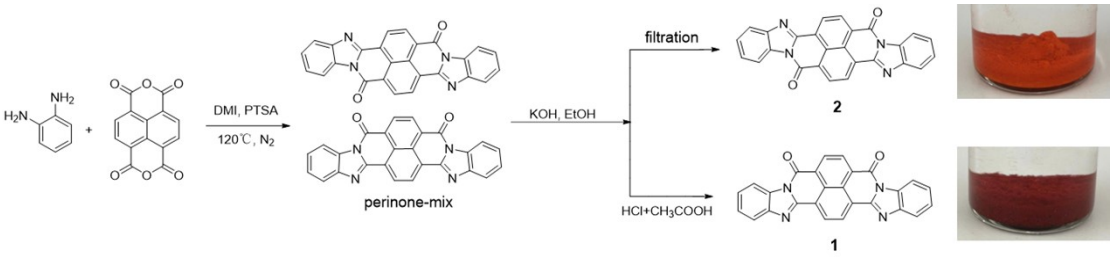

Scheme S1 The synthetic route of perinone-mix, *cis*-perinone (**1**) and trans-perinone (**2**).

Synthesis of perinone-mix: A mixture of naphthalenetetracarboxylic dianhydride (1.20 g, 4.49 mmol), 1,2-phenylenediamine (1.0 g, 9.25 mmol), *p*-Toluenesulfonamide (2.56 g, 14.95 mmol) and trifluoroacetic acid (TFA, 1.1 mL) was stirred in 1,3-Dimethyl-2-imidazolidinone (DMI, 20 mL) under N_2 atmosphere at 120 °C for 22 h. After cooling down to room temperature, the precipitate was collected by filtration, washed with dimethylformamide (DMF), H_2O, ethanol, acetone, and dried under vacuum at 100 °C overnight, to give perinone-mix as deep-red solid in 95 % yield.

Separation of two isomers: 3 g potassium hydroxide (KOH) was dissolved in 30 mL ethanol with a stirrer. The prepared perinone-mix (1 g, 2.42 mmol) was added to the alkaline ethanol solution, and refluxed for 2 h. After cooling down to room temperature, the precipitate was collected by filtration, washed with alkaline solution, ethanol and dried under vacuum at 100 °C to obtain brilliant orange *trans*-perinone (**2**). The resulting filtrate was treated with a mixture of hydrochloric acid and acetic acid (4 ml HCl and 1 ml AcOH in 30 ml H_2O), and the solid was gradually formed. The precipitate was collected by filtration, washed with H_2O and ethanol, and dried under vacuum at 100 °C overnight, to give *cis*-perinone (**1**) as blueish-red powder.

Electrode preparation: The perinone electrode was thoroughly mixed by perinone, acetylene black and PTFE in a weight ratio of 70:20:10, with ethanol as the solvent. The mixture was sonicated for 1 h until all the components were uniformly dispersed in ethanol. Ti foil was cut into a circular shape with diameter of 1 cm and then placed over a hot plate (80 °C). The mixture was dropped onto the Ti foil. Then the electrode was further dried in an oven at 80 °C for 12 h before use. The loading of active perinone in each electrode is

controlled as 1.5~2 mg/cm^2. The high-loading perinone electrode (26 mg/cm^2) was prepared by mixing **1**, acetylene black and PTFE in a weight ratio of 70:20:10, with ethanol as the solvent, continuously grinding the mixture until the mixture forms a homogeneous agglomerate. The agglomerate is driven into a film of uniform thickness and dried overnight. The counter electrode was activated carbon (AC), which mixed by acetylene black and PTFE in a weight ratio of 90:5:5.

The MnO_2@CC electrode was prepared by an electrodeposition method. Typically, a piece of commercialized carbon cloth (CC) with size of 1×1 cm was immersed into the acid electrolyte containing Mn^{2+} (0.5 M H_2SO_4 + 2 M $MnSO_4$). MnO_2 electrodeposition was performed within a typical three-electrode system, where the carbon cloth was used as the working electrode, activated carbon electrode as the counter electrode, and Ag/AgCl electrode as the reference electrode. The three-electrode cell was galvanostatic charged at a constant current of 1 mA with different deposition times. The as-obtained MnO_2@CC electrode was dried at 80 °C for 5 h in vacuum oven.

Electrochemical tests: The electrochemical performances of the perinone electrode, AC electrode and MnO_2@CC electrode in the acid electrolytes were investigated, respectively, by a typical three-electrode system, in which Ag/AgCl electrode and activated carbon film electrode were served as reference and counter electrodes, respectively. 0.5 M H_2SO_4 and 2 M $MnSO_4$ + 0.5 M H_2SO_4 solutions were used as electrolyte, respectively. The cyclic voltammetry (CV) curves, linear-sweep voltammetry (LSV) curves investigation and galvanostatic charge/discharge curves were all collected using CHI760 electrochemical workstation. The galvanostatic charge/discharge (GCD) tests were collected on the LAND CT2001A battery system. The current density and capacity of perinone electrodes were calculated based on the active mass of perinone. All experiments are performed at room temperature.

Material Characterization: The solution ^{1}H and ^{13}C nuclear magnetic resonance (NMR) were conducted on a 400 MHz NMR spectrometer (Bruker AV400) to define the structure of perinone-mix, **1** and **2**. The morphology and microstructure of three perinone molecules were observed by Hitachi S4800 scanning electron microscope (SEM) equipped with energy dispersive X-ray (EDX). FTIR was collected through Thermo ScientificNicolet 6700 FTIR equipped with an mercury cadmium telluride (MCT) detector cooled with liquid nitrogen. *In-situ* FTIR equipment was received from Linglu Instruments (Shanghai) Co.,Lt in a three- electrode cell, in which platinum wire and Ag/AgCl were used as opposite electrode and reference electrode, respectively. The CV measure was conduced at a scan rate of 0.2 mV/s. Raman spectrum was collected through a spectrophotometer (Renishaw inVia Reflex, Renishaw) with a wavelength of 785 nm. A three-electrode cell containing active material on Ti mesh (working electrode), activated carbon counterelectrode and Ag/AgCl electrode was assembled, and tested at a CV scan rate of 0.2 mV/s. The X-ray photoelectron spectra (XPS) were collected on Shimadzu AXIS SUPRA spectrograph under vacuum (2×10^{-9} Pa) with Al Kα radiation. XRD tests were collected on a Bruker D8 Advance X-ray diffractometer with 2θ ranging from 5° to 60°. The specific surface area was measured by using a gas adsorption instrument (BELSORP, MAX), and the nitrogen adsorption and desorption curves were plotted. The degassing temperature was 120 °C, vacuum degassing was carried out for 6 h, the test temperature was 77 K, and the BET

specific surface area was calculated within the range of P/P_0 = 0.05-0.30. The pore size distribution was analyzed by the BJH method (desorption side).

The spectroelectrochemical experiments were performed in the optical ESR cavity (ER 4104OR, Bruker Germany). EPR spectra were recorded by the EMX X-band CW spectrometer (Bruker, Germany). An NMR teslameter (ER036TM, Bruker, Germany) was used for precise *g* value determination. The UV−vis−NIR spectra were measured using the Avantes spectrometer AvaSpec-2048×14-USB2 with the CCD detector and AvaSpec-NIR256-2.2 with the InGaAs detector applying the AvaSoft 7.5 software (Avantes, The Netherlands). A light source Avantes Avalight-DH-S-BAL was used. Both, the ESR spectrometer and the UV−vis−NIR spectrometer are linked to a HEKA potentiostat PG 390 which triggers both spectrometers. Triggering is performed by the software package PotMaster v2×90 (HEKA Electronik, Germany). Each UV−vis−NIR spectrum was collected relative to that of the neutral (uncharged) compound at the initial potential. For standard in situ ESR/UV−vis−NIR spectroelectrochemical experiments, a three-electrode EPR flat cell was used. A ITO (the material was drop coated on the electrode from ethanol suspension) as working electrode, an AgCl coated silver wire as pseudo reference electrode, and a platinum wire as counter electrode were used in spectroelectrochemical experiments. 0.5 M H_2SO_4 was used as a supporting electrolyte. The measurements were conducted at a scan rate of 1.5 mV/s.

Theoretical Calculations: The DFT calculations were carried out using Gaussian 16 software[1] package. The molecular configurations were fully optimized at B3LYP level of theory with 6-31++G(d,p) basis set. The solvation effect using implicit solvation model (SMD) for a precise simulation of the experimental conditions in water solution is also considered in the optimization. All of the optimized structures were characterized to be a true local energy minimum on potential energy surfaces without imaginary frequencies.The energy levels of HOMO and LUMO of abovementioned molecules were obtained during the same process. All the calculated results of MPP, MESP, LOL-π, NICS and IRI were performed with Multiwfn 3.3.9 programs[2] and the visualization of MESP plots were carried out by Visual Molecule Dynamics (VMD) software. Anisotropy of induced current density (AICD) plots were calculated by Herges' method.

Crystallographic data refinement was conducted using the Reflex module to ensure accurate optimization of the crystal structure model. The refinement process comprised 10 iterative cycles, with each cycle involving 30 evaluations per degree of freedom (DOF). This extensive evaluation strategy was implemented to enhance the precision and stability of the parameter adjustments, thereby minimizing the risk of converging to local minima and ensuring a robust refinement outcome. Data collection was performed with a step size of 0.020°, providing high-resolution sampling of the diffraction pattern. This fine step size facilitated the detailed characterization of peak shapes and positions, which is critical for achieving precise refinement results.

Supplementary Methods

Calculation of theoretical capacity and the electron-transfer numbers: The theoretical capacity (Q) of perinone can be calculated as follows:

$$Q = \frac{nF}{3.6M}$$

where Q is the theoretical specific capacity (mAh/g), n is the theoretical electron-transfer numbers, F is the Faraday constant (96485 C/mol) and M is the relative molecular mass. Then the electron-transfer numbers (n) can be calculated by following equation:

$$n = \frac{3.6QM}{F}$$

EQCM measurement: The *in-situ* mass change during the discharge process by CV scan at 5 mV/s was detected by a QCM-401 electrochemical quartz crystal microbalance (EQCM, Biolin Scientific). Gold sensors coated with a uniform and thin **1** and **2** film serve as the working electrodes, respectively. The reference and counter electrodes used Ag/AgCl and Pt plate, respectively. The electrolyte was 0.5 M H_2SO_4. The solution volume above the crystal was 100 μL. In parallel with QCM-401, the electrochemical data were acquired by the versa studio-software in the electrochemical workstation (CHI 760E).

EQCM registers the mass change (Δm) versus charge change (d_q) in the perinone electrode attached to the quartz surface. Such a change should follow the Sauerbrey equation:

$$\Delta m = \frac{\sqrt{\rho\mu}}{2f} \times \Delta f = -Cf \times \Delta f$$

where ρ_q is the density of quartz (2.648 g/cm^3), μ_q is the shear modulus of quartz (2.947 × 1011 g/cm s^2), f_0 is the fundamental resonance frequency of the quartz, C_f is the sensitivity factor. Δm and Δf are the mass change and frequency change, respectively. C_f is obtained by calculating the relation based on the frequency and mass change (measured by balance) between clean quartz and the coated electrodes.

The value of the calibration constant used in this work is 17.7 ng/Hz, and the molar weight of the charge carrier (M_w) is calculated by the Equation below:

$$Mw = \frac{\Delta mnF}{\Delta Q} = \frac{Cf(-\Delta f)nF}{\Delta Q}$$

where F is Faraday constant (96485.33 C/mol) while n is the valence number of the ion. ΔQ is the Coulombs of charge passed through during the CV process.

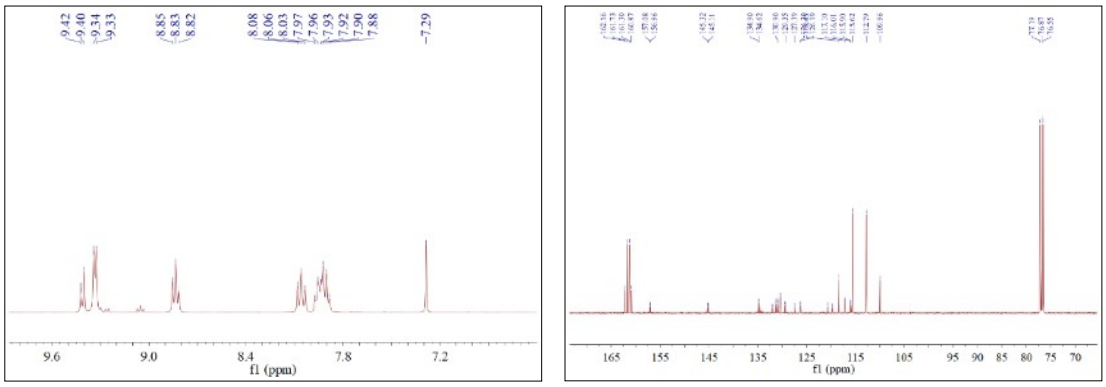

Figure S1 ^{1}H NMR and ^{13}C NMR (400 MHz, $CDCl_3$:TFA=6:1) spectrum of **perinone-mix**.

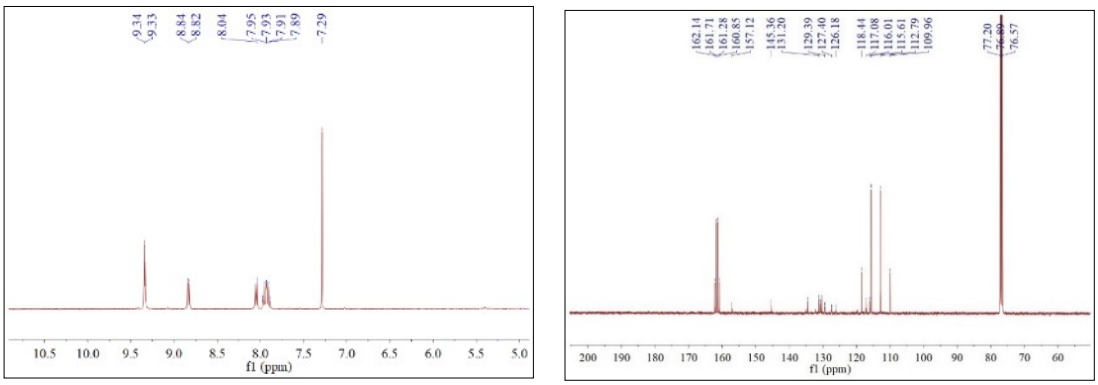

Figure S2 ^{1}H NMR and ^{13}C NMR (400 MHz, $CDCl_3$:TFA=6:1) spectrum of **1**.

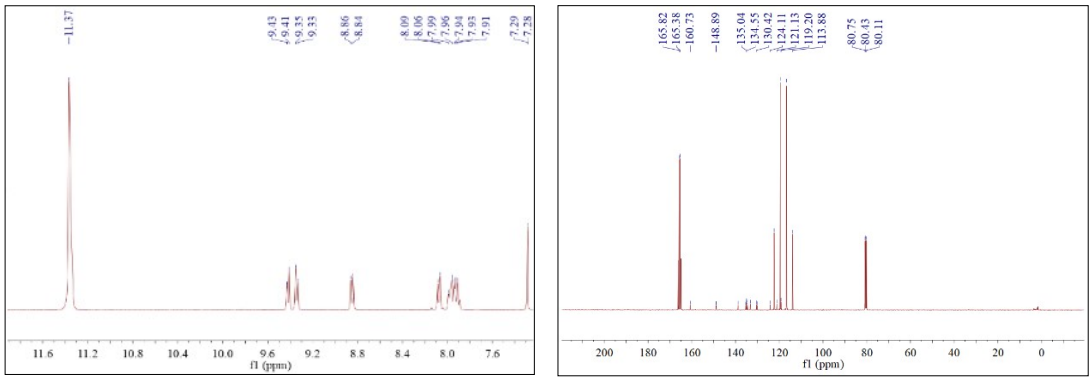

Figure S3 ^{1}H NMR and ^{13}C NMR (400 MHz, $CDCl_3$:TFA=6:1) spectrum of **2**.

Table S1 Crystallographic Parameters for **1** and **2**.

Compd.	**1**	**2**
CCDC number	1872270	214992
formula	$C_{26}H_{12}N_4O_2$	$C_{26}H_{12}N_4O_2$
M_w	412.4	412.4
crystal system	monoclinic	monoclinic
space group	P 1 21/c 1 (14)	P 1 21/c 1 (14)
Molecular symmetry	C_{2v}	C_i
a [Å]	12.146(4)	11.199(1)
b [Å]	4.7996(12)	4.8120(6)
c [Å]	27.494(7)	16.091(2)
α [°]	90	90
β [°]	95.821	96.816
γ [°]	90	90
V [Å^3]	1725.8(8)	861.01(20)
Z	4	2
ρ_{calcd} [g cm^{-3}]	1.587	1.591

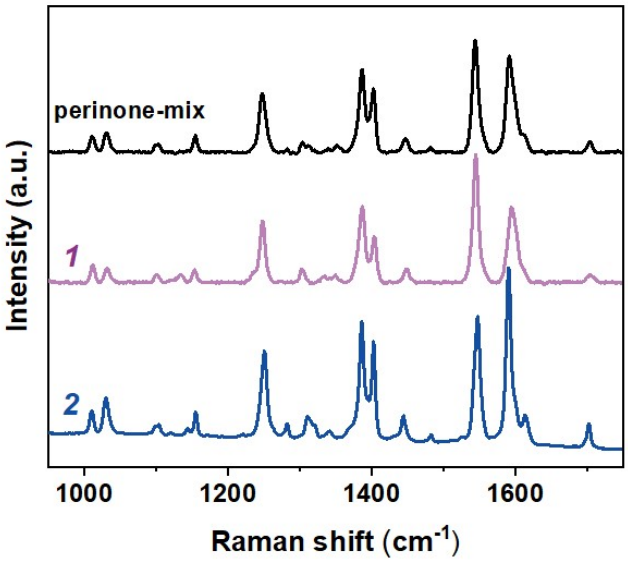

Figure S4 Raman spectrum (785 nm) of **perinone-mix**, **1** and **2**.

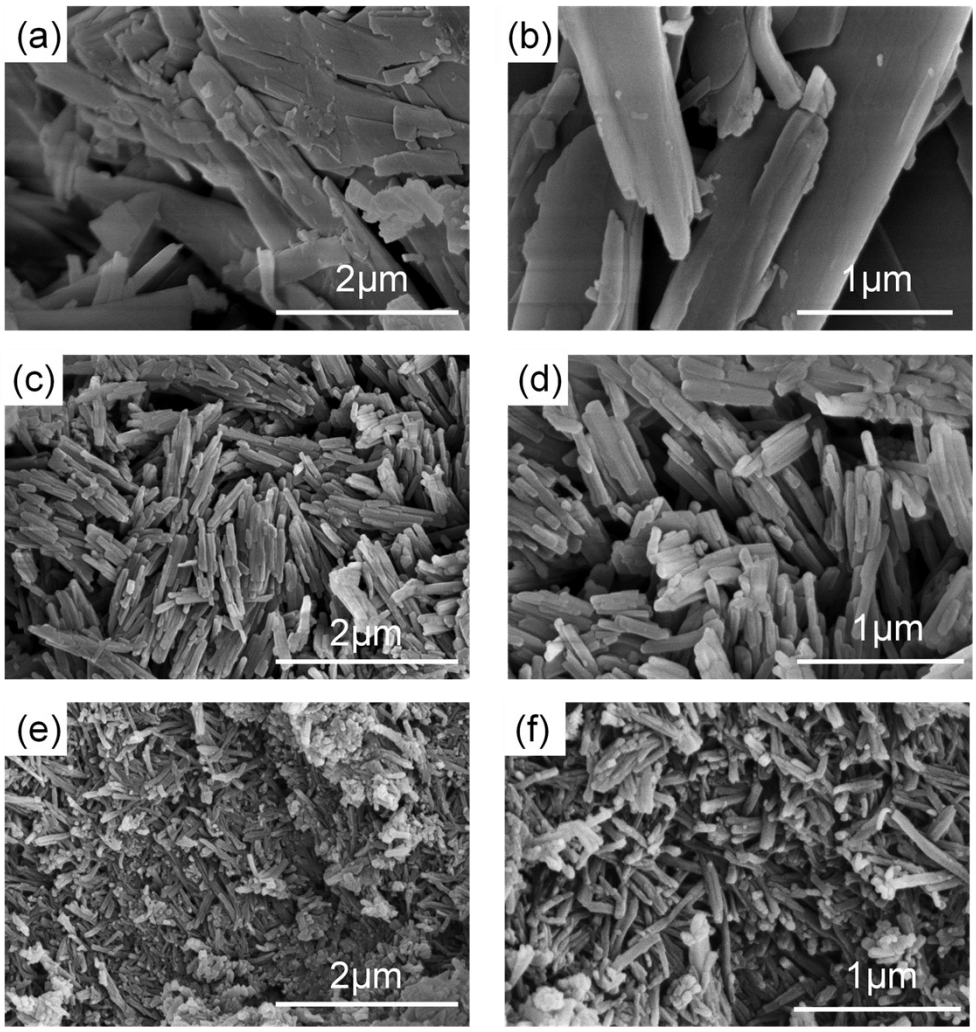

Figure S5 (a, b) SEM images of **perinone-mix**. (c,d) SEM images of **1**. (e,f) SEM images of **2**.

Table S2 HOMO-LUMO comparison of organic compounds.

Compd.	Structure	HOMO/ eV	LUMO/eV	△E/ eV
NTCDI	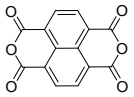	-7.17	-3.66	3.52
DAP	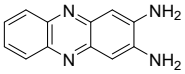	-5.82	-2.46	3.37
PNZ	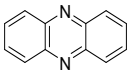	-6.40	2.83	3.57
PTO	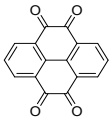	-7.15	-3.81	3.34
HATN	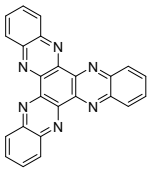	-6.74	-3.14	3.60
PT	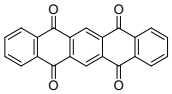	-7.55	-3.759	3.79
1	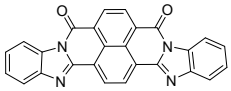	-6.14	-3.58	2.56
2	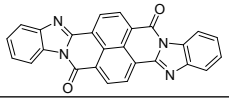	-6.34	-3.56	2.78

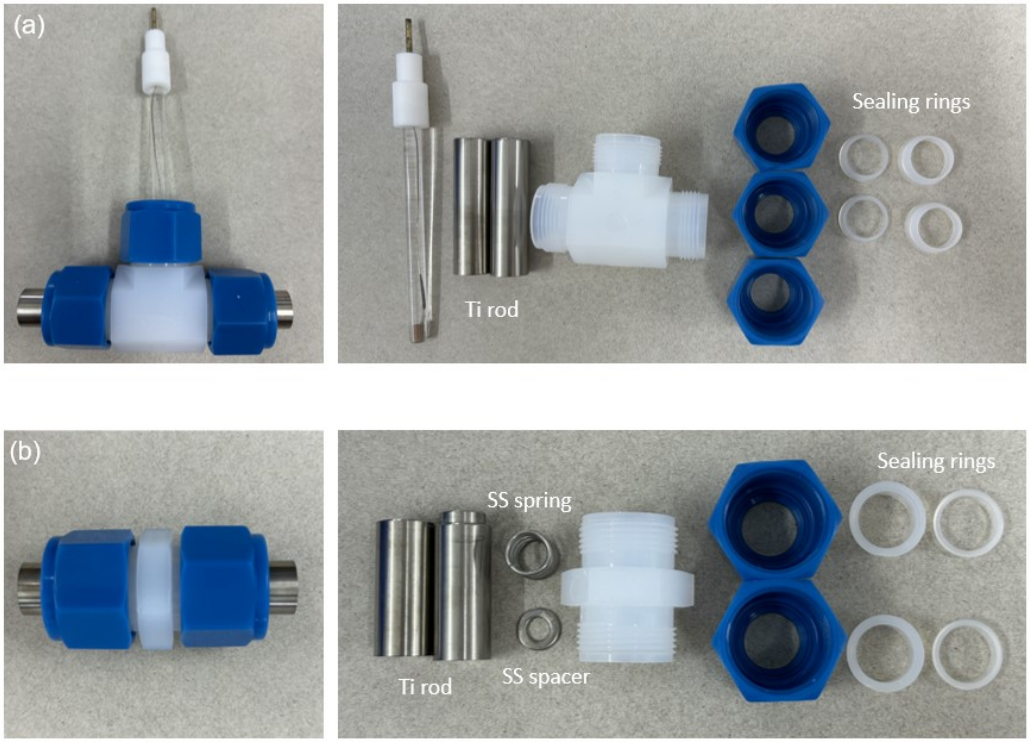

Figure S6 Photographs of home-made Swagelok cells in (a) three-electrode and (b) two-electrode configurations.

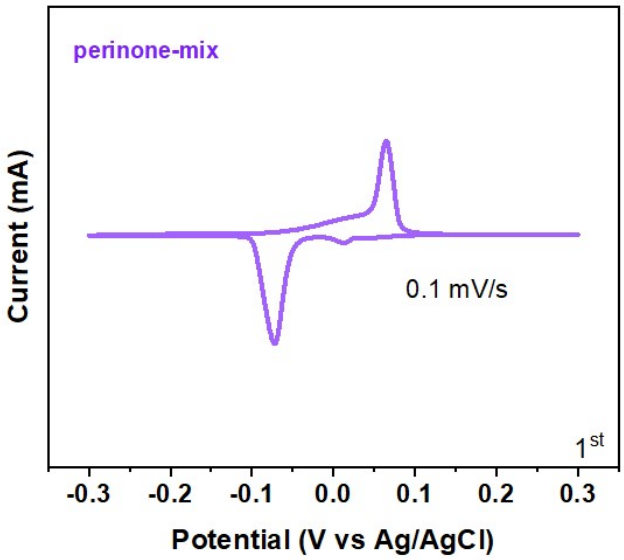

Figure S7 CV curves (1st) of **perinone-mix** at a scan rate of 0.1 mV/s.

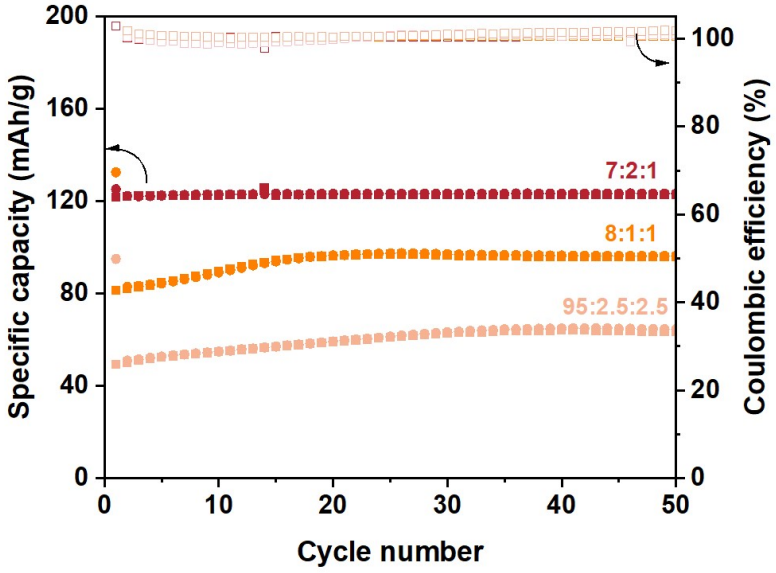

Figure S8 Cycling performance of **1** electrode with different ratio of active materials.

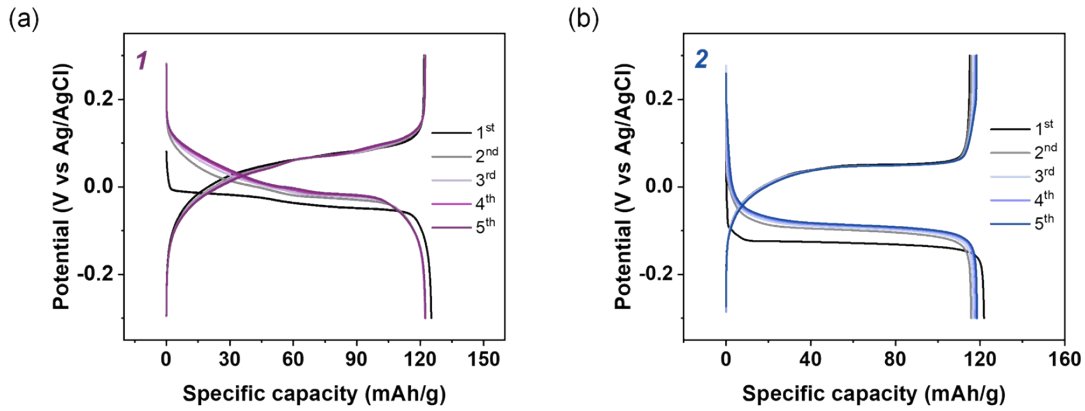

Figure S9 The initial 5-cycles charge-discharge curves of **1** (a) and **2** (b) at 0.1 A/g.

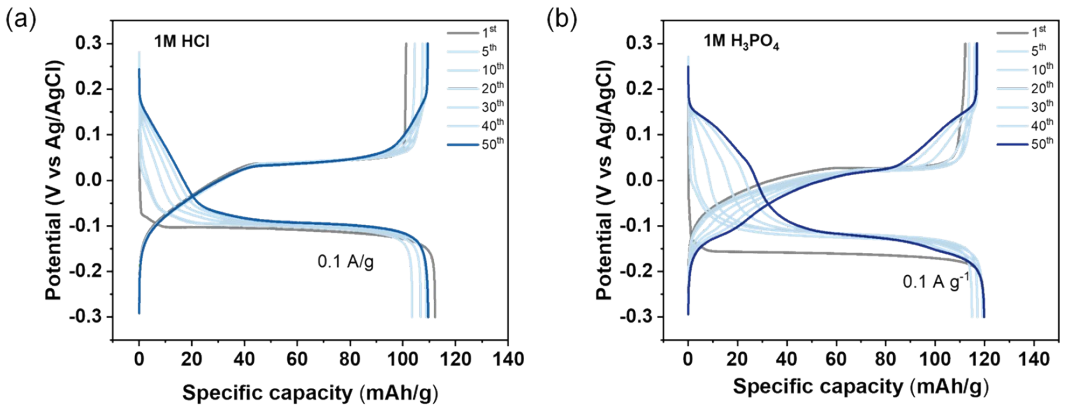

Figure S10 The charge-discharge curves of **2** in 1 M HCl (a) and 1 M H_3PO_4 (b) at 0.1 A/g.

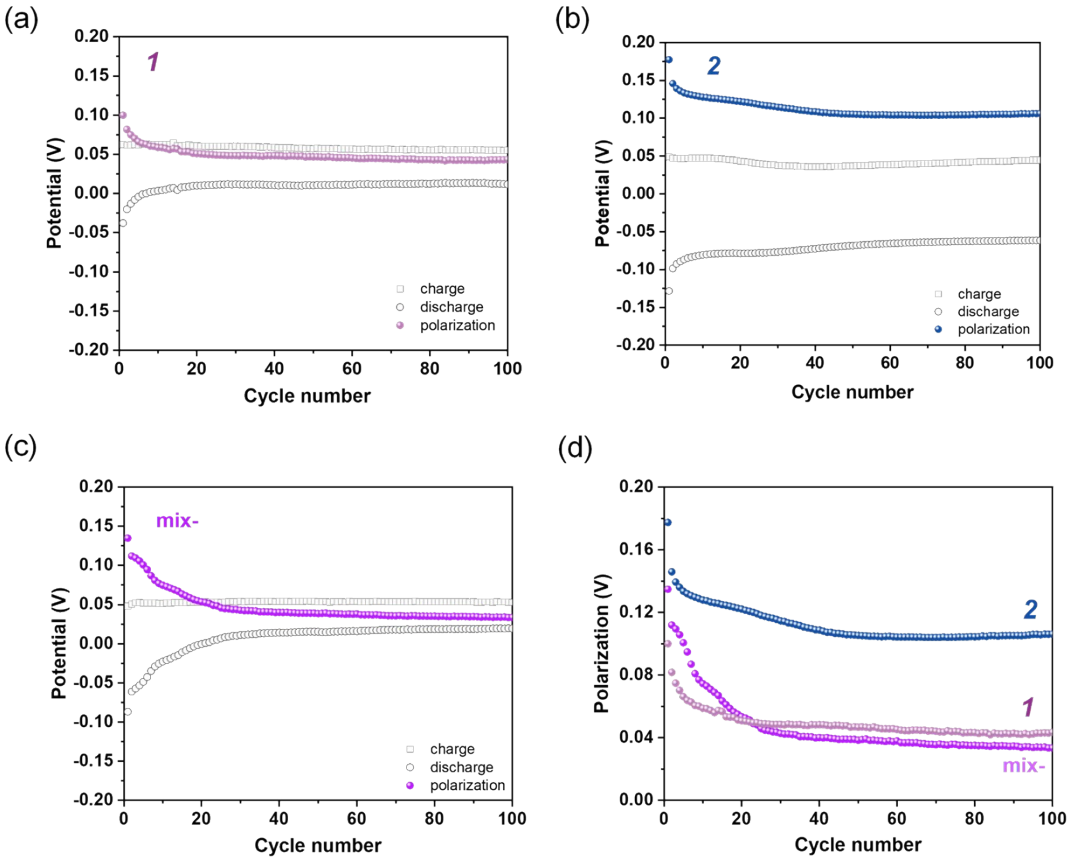

Figure S11 Comparison of overpotentials of perinone isomers during charge-discharge cycles.

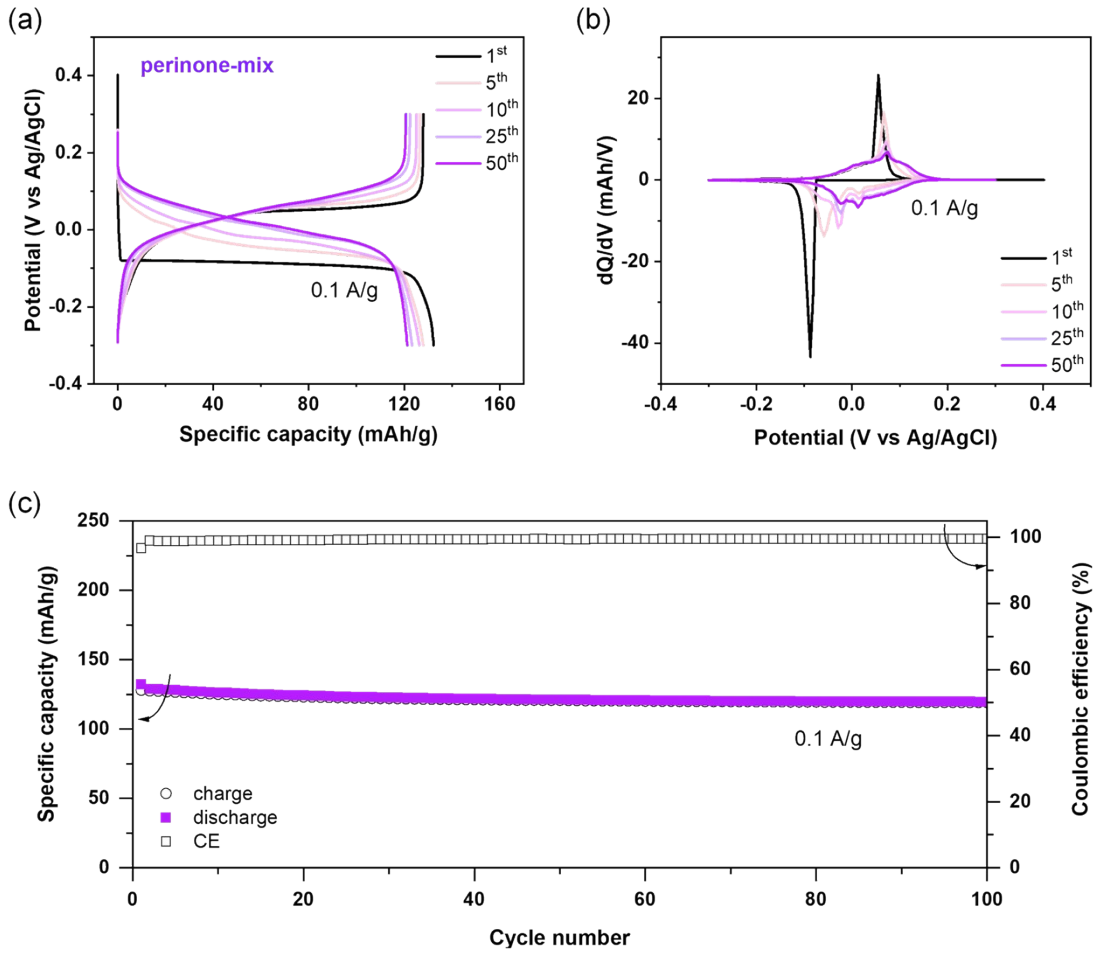

Figure S12 Electrochemical performance of **perinone-mix**. (a) CV curves (1st) at a scan rate of 0.1 mV/s. (b) Charge–discharge curves of different cycles at 0.1 A/g. (c) The dQ/dV curves at 0.1 A/g. (d) Cycling performance at 0.1 A/g.

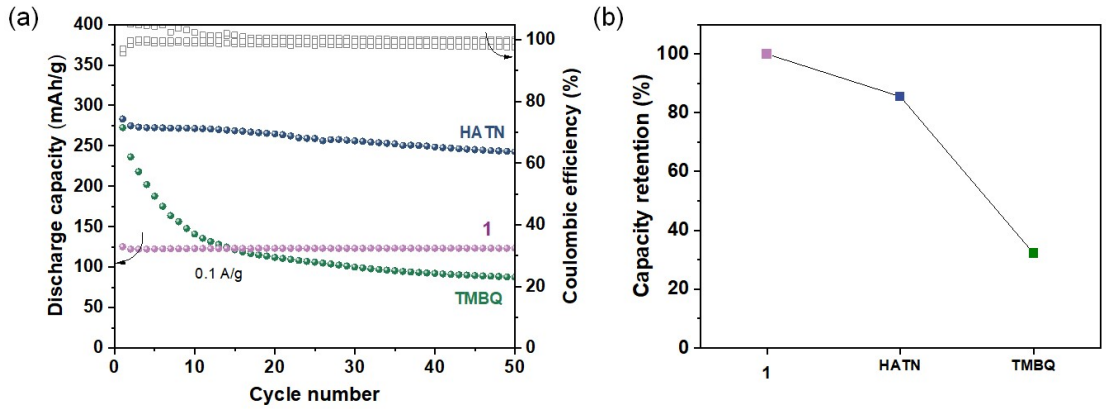

Figure S13 (a) Cycling performance of **HANT**, **TMBQ** and **1** electrode in 0.5M H_2SO_4 at 0.1 A/g; (b) Capacity retention of **HANT**, **TMBQ** and **1** electrode in 50 cycling.

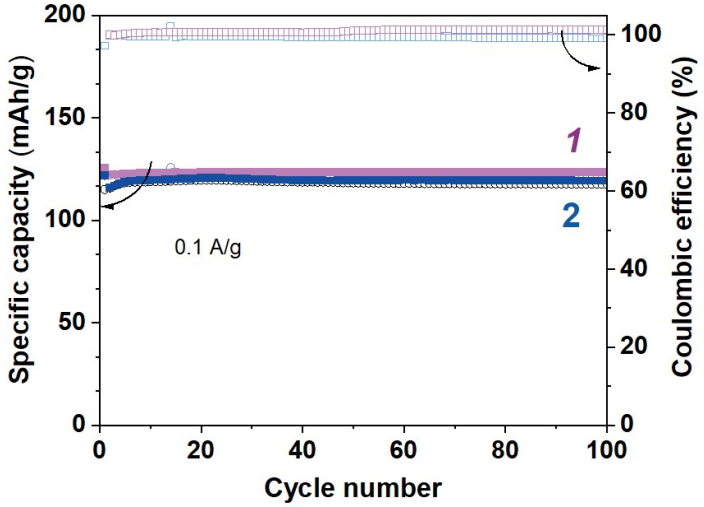

Figure S14 (a) Cycling performance of **1** and **2** electrode at 0.1 A/g in 100 cycling.

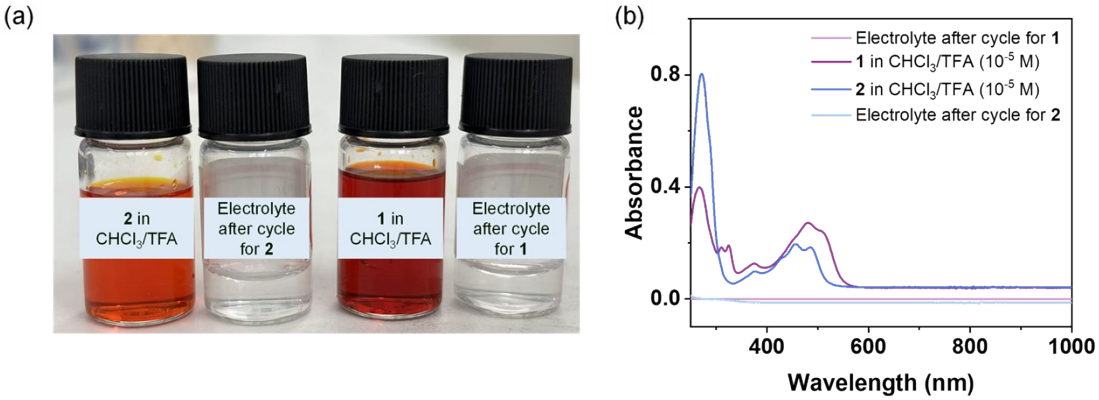

Figure S15 (a) Optical photographs of compound **1** and **2** in $CHCl_3$/TFA (v:v=6:1) and the electrolytes after cycle for **1** and **2**.

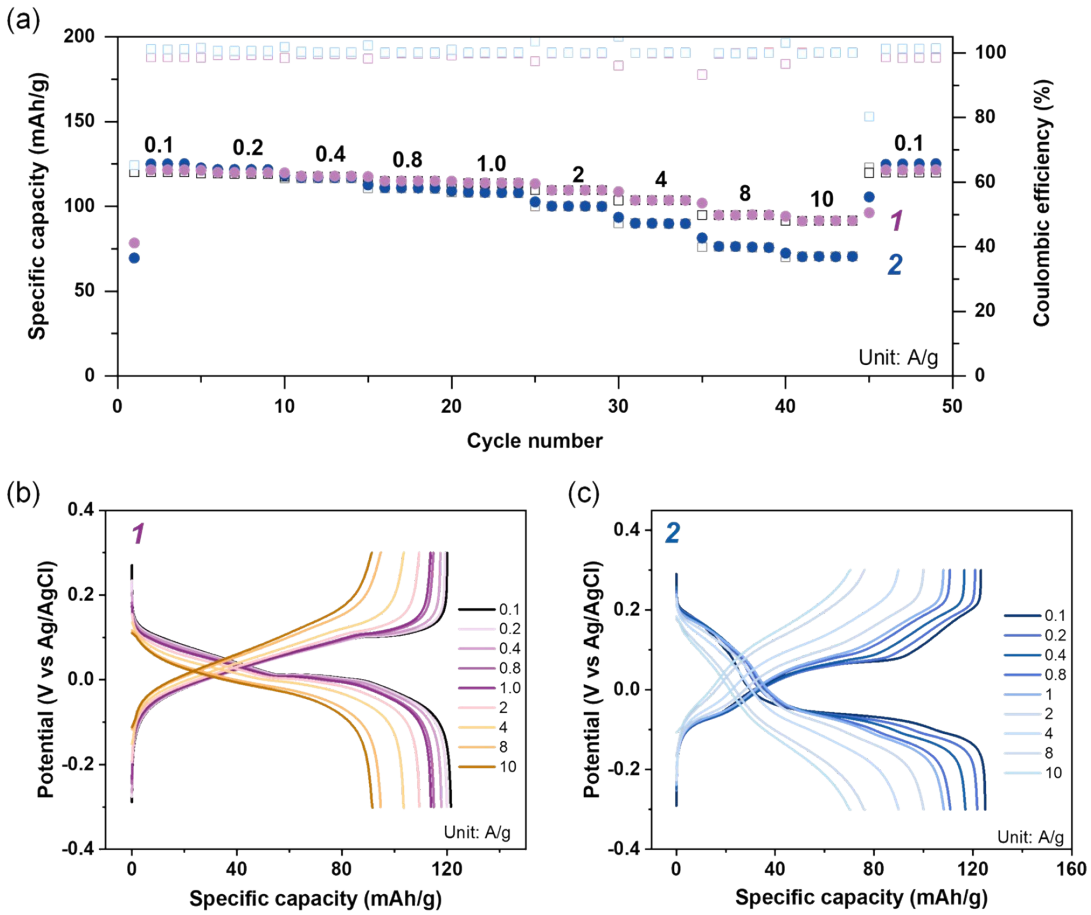

Figure S16. (a) Rate performance of **1** and **2** at 0.1~10 A/g; (b) Charge–discharge curves of **1** at 0.1~10 A/g; (c) Charge–discharge curves of **2** at 0.1~10 A/g.

1 performs better than **2** at high current densities. This can be explained by the following reasons: (1) **1** possesses a narrower HOMO-LUMO gap (2.56 eV) than **2** (2.78 eV) and many other organic compounds (>3 eV; *Chem. Eng. J.* **2025,** *510*, 161650), indicates superior charge transport efficiency; (2) larger hydrated proton species inserted in **2** than **1** may be another reason for inferior reaction kinetics; (3) **1** shows a smaller size and larger surface area (40 m^2/g vs 25 m^2/g) as confirmed by the SEM and BET results (Figure S17). Reason (1), (2) and (3) is expected to strongly correlate with isomerism.

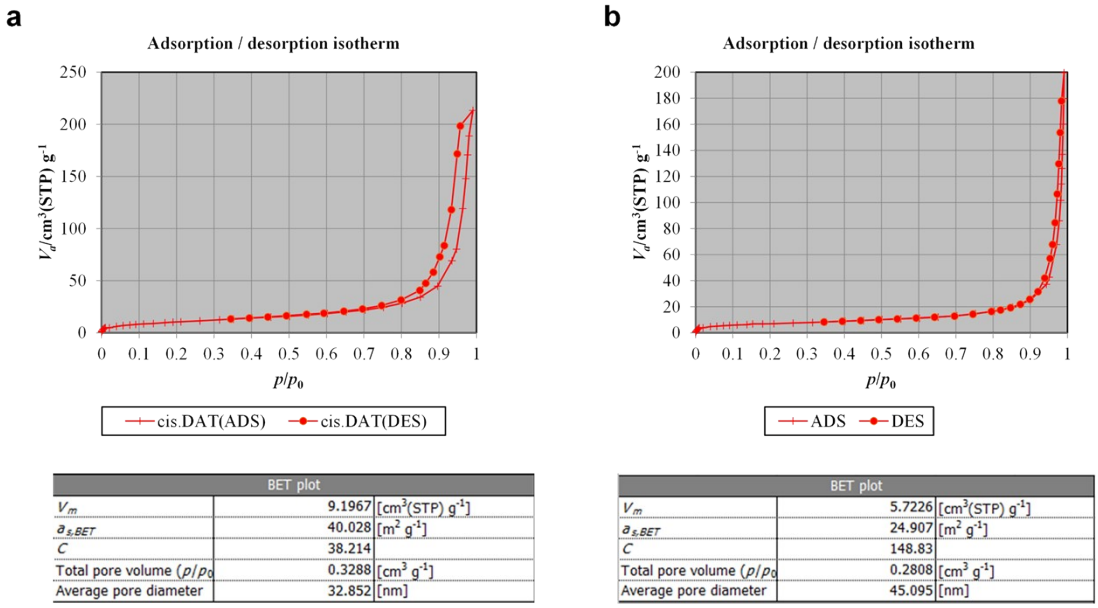

BET plot		
V_m	9.1967	[cm^3(STP) g^{-1}]
$a_{s,BET}$	40.028	[m^2 g^{-1}]
C	38.214	
Total pore volume (p/p_0	0.3288	[cm^3 g^{-1}]
Average pore diameter	32.852	[nm]

BET plot		
V_m	5.7226	[cm^3(STP) g^{-1}]
$a_{s,BET}$	24.907	[m^2 g^{-1}]
C	148.83	
Total pore volume (p/p_0	0.2808	[cm^3 g^{-1}]
Average pore diameter	45.095	[nm]

Figure S17. Brunauer-Emmett-Teller (BET) surface area test of **1** (a) and **2** (b) powder.

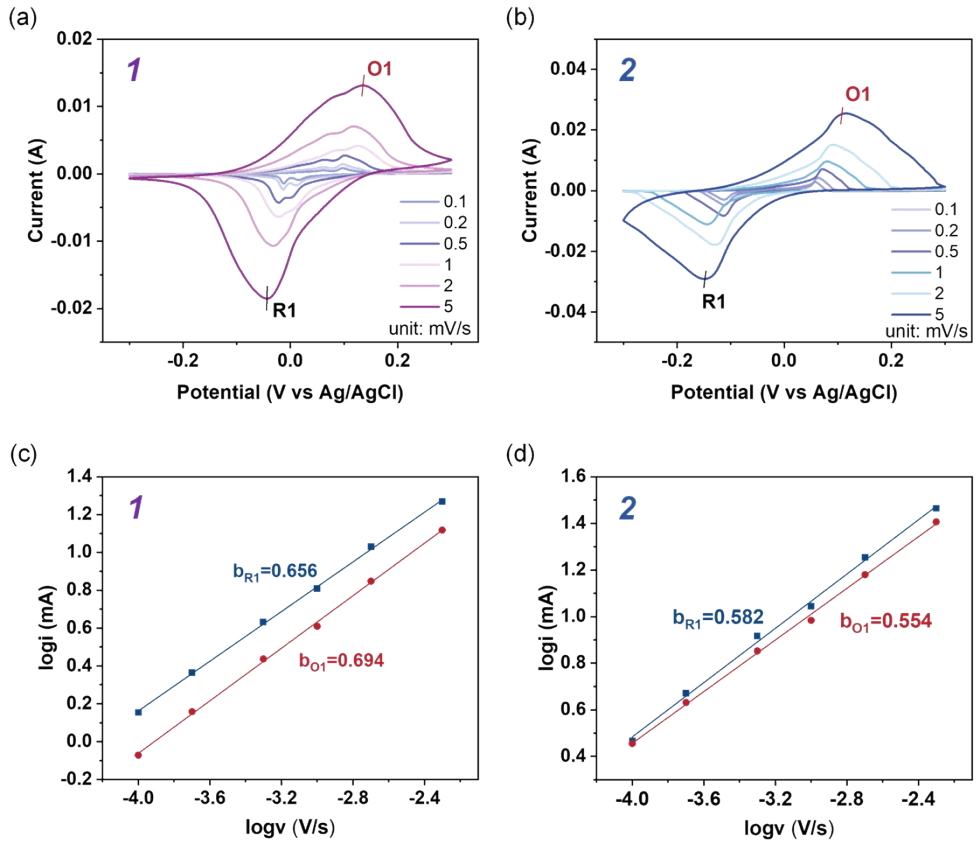

Figure S18 (a) CV curves at various scan rates of **1** electrode. (b) CV curves at various scan rates of **2** electrode. (c) log(i) vs.log(v) plots according to the CV curves of **1** electrode. (d) log(i) vs.log(v) plots according to the CV curves of **2** electrode.

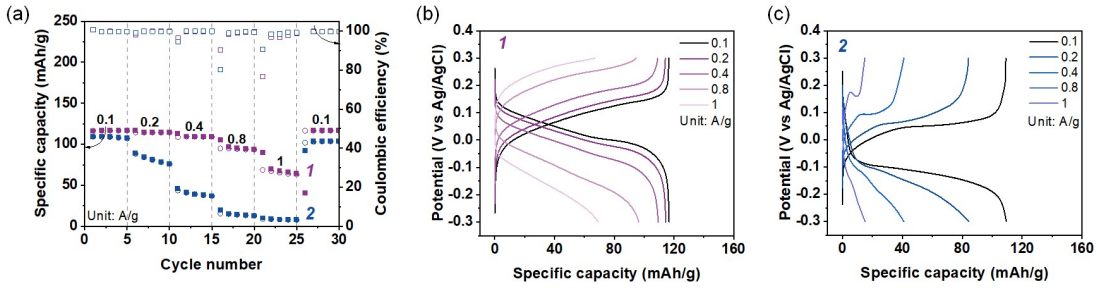

Figure S19 (a) Rate performance of **1** and **2** at 0.1~1 A/g under high areal mass loading of 28.3 and 26.1 mg/cm^2, respectively. (b) Charge-discharge curves of **1** at 0.1~1 A/g. (c) Charge–discharge curves of **2** at 0.1~1 A/g.

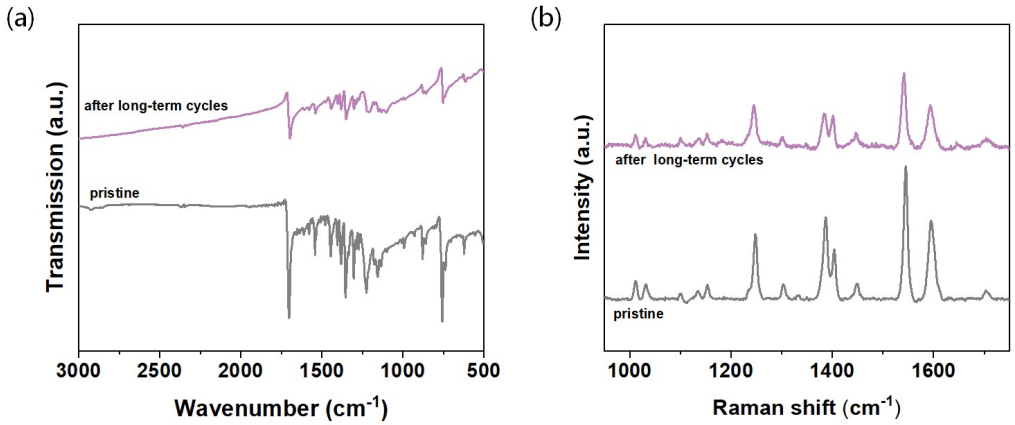

Figure S20 (a) FTIR spectra of **1** electrode before (gray) and after (orange) long-term cycling test; (b) Raman spectra of **1** electrode before (gray) and after (orange) long-term cycling test.

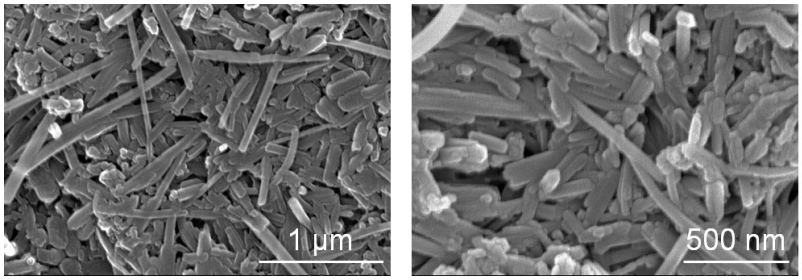

Figure S21 SEM images of **1** electrode after long-term cycling.

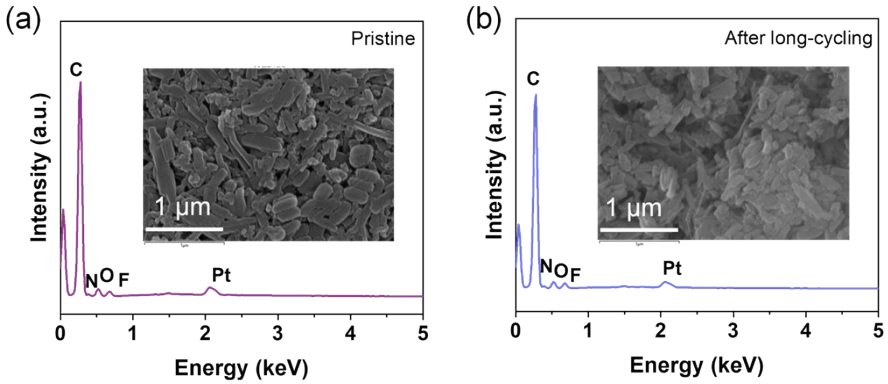

Figure S22 EDX results of pristine **1** electrode (a) and after long-term cycling (b).

Table S3 Cycling stability comparison of proton-storage organic materials

Materials	Electrolyte	Current density	Capacity (mAh/g)	Cycling performance (retention)	Ref.
PTO		2.5C	118	1000 (78%)	[3]
PTCDA	1M H_2SO_4	1 A/g	85	120 (71%)	[4]
BQPH		10 A/g	200	1000 (82%)	[5]
PO	$ZnSO_4$	1 A/g	100	500 (94%)	[6]
HATN	2M $MnSO_4$ + 2M H_2SO_4	5 A/g	163	3500 (66%)	[7]
PI	2M $MnSO_4$ + 2M H_2SO_4	1 A/g	80	3500 (66%)	[8]
2,6-DHN	0.5M H_2SO_4	5 A/g	90	1000 (80%)	[9]
pDTP-AQ	1M H_2SO_4	10C	/	1000 (83%)	[10]
pDTP-NQ	1M H_2SO_4	10C	/	1000 (67%)	[10]
AN-TA	2 M H_2SO_4	1 A/g	120	500 (81%)	[11]
AN-PA	2 M H_2SO_4	1 A/g	145	500 (87%)	[11]
PNAQ	0.5M H_2SO_4	0.6 A/g	91.6	500 (70%)	[12]
PUQ	0.5M H_2SO_4	5 A/g	94.2	1000 (82%)	[13]
1	**0.5 M H_2SO_4**	**10 A/g**	**90**	**8000 (100%)**	**This work**

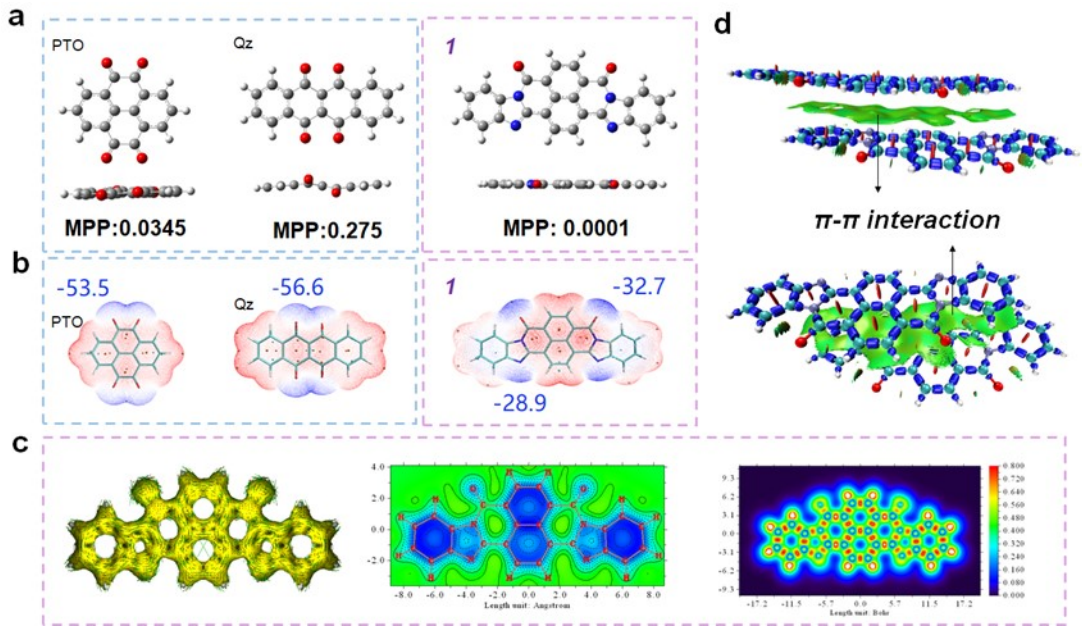

Figure S23 (**a**) The calculation of molecular planarity parameter (MPP) and electrostatic potential surfaces for PTO, Qz and **1**. (b) The electrostatic potential surfaces for PTO, Qz and **1**. (c) AICD plots, NICS_zz analysis and LOL-π map (from left to right) for **1**. (d) Isosurface map of IRI of two **1** molecules in two layers.

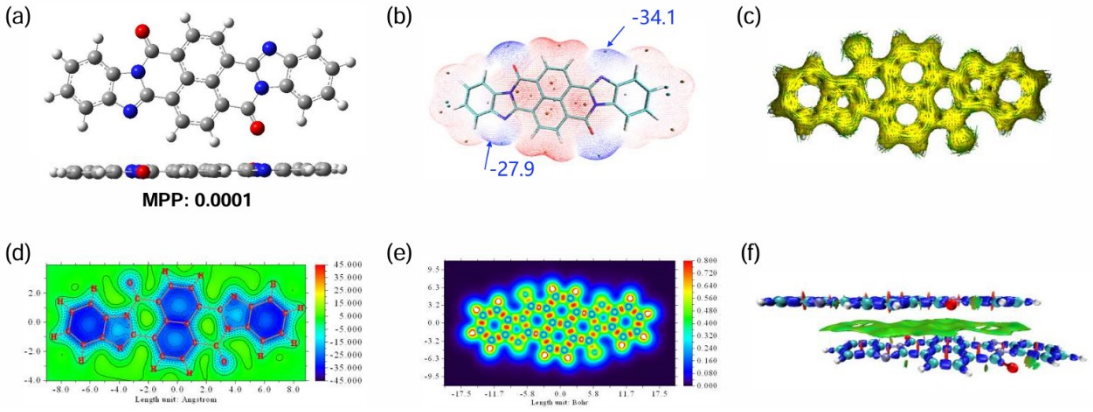

Figure S24 DFT calculations of **2**. (a) The optimized structure and MPP value; (b) Electrostatic potential surfaces; (c) AICD plots; (d) NICS_zz analysis; (e) LOL-π map; (f) Isosurface map of IRI analysis

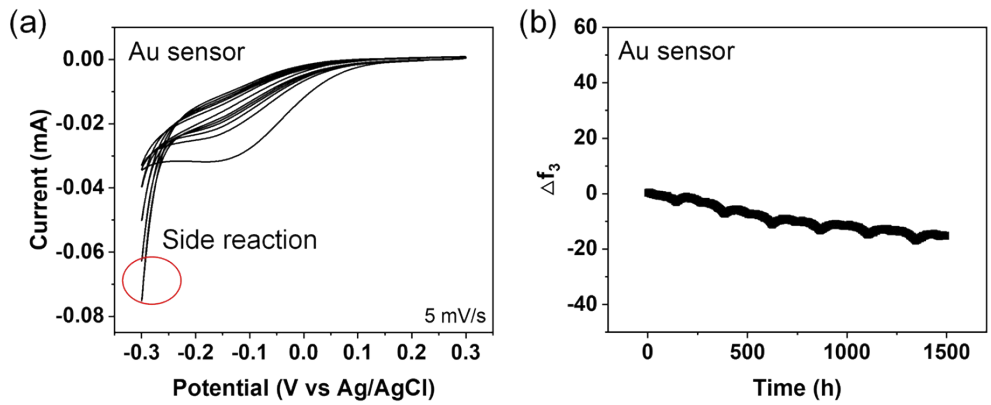

Figure S25 (a) cyclic voltammetry measurement of gold sensor in 0.5M H_2SO_4 at 5 mV/s. (b) Time-dependent changes in frequency of gold sensor.

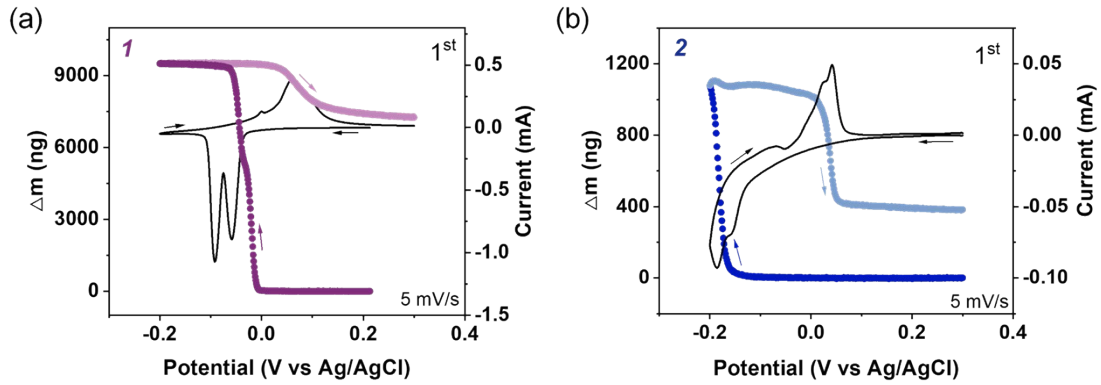

Figure S26 Mass profiles for **1** (c) and **2** (d) during 1st CV.

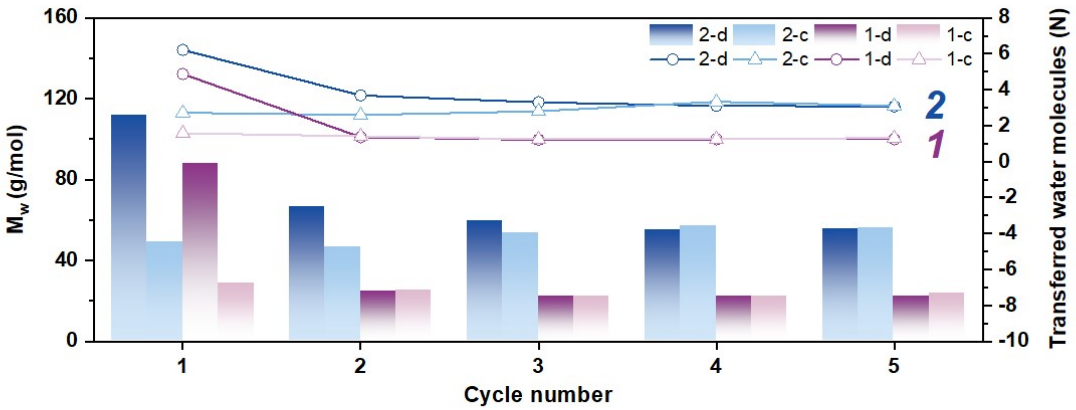

Figure S27 The M_w and the corresponding number of water molecules transferred during the redox reaction for **1** and **2**.

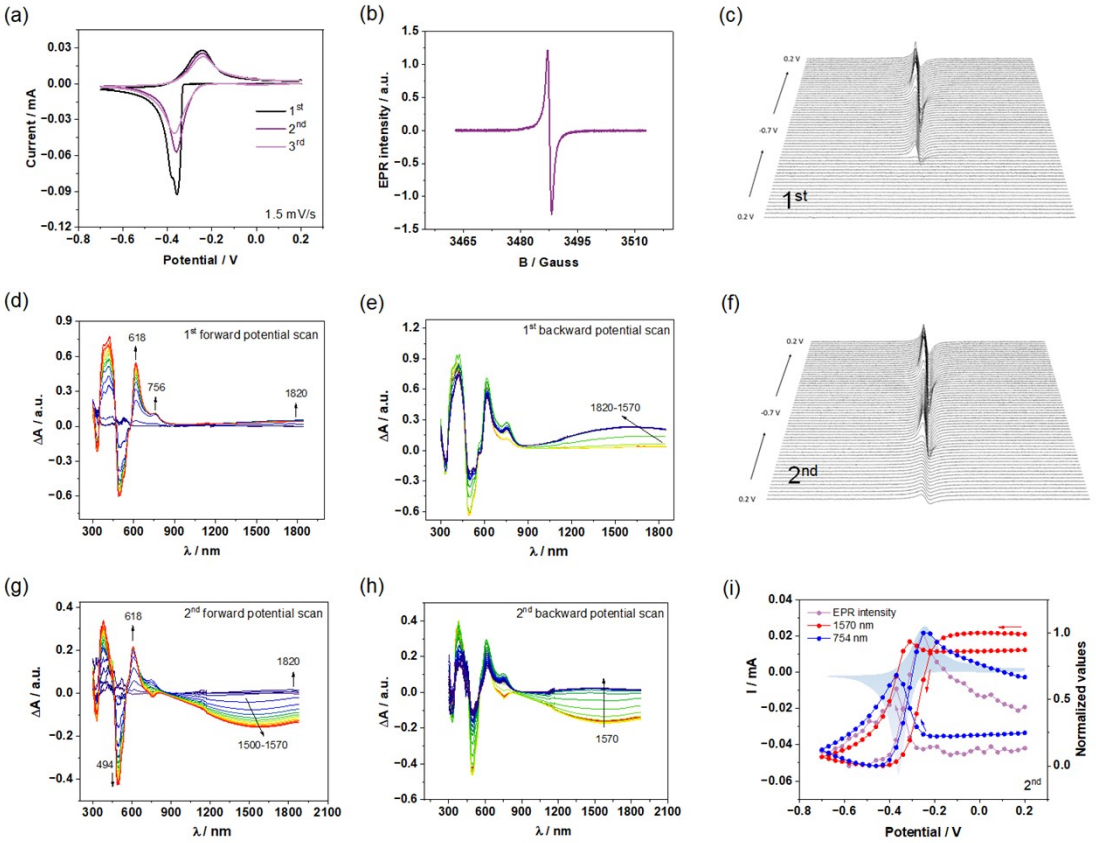

Figure S28 Electrochemistry (EC) and spectroelectrochemistry (SEC) measurements on **1** electrode. (a) CV curves at 1.5 mV/s. (b) EPR spectrum of **1** radical anion. Evolution of EPR spectra as a function of potential recorded during the 1st cycle (c) and 2nd voltammetric cycle (f). UV–vis–NIR spectra of **1** measured during reduction (d) and re-oxidation (e) (1st cycle). UV–vis–NIR spectra of **1** measured during reduction (g) and re-oxidation (h) (2nd cycle). (i) Dependence of the EPR signal intensity as well as the intensity of the selected absorption bands on applied potential (2nd cycle).

In the forward potential scan, the UV-vis-NIR spectra show an absorption band at 756 nm and NIR one at ca. 1800 nm which potential dependence coincides with that of the EPR signal. Upon the re-oxidation process, the broad NIR band blue shifts from 1800 to 1570 nm and reaches a maximum at the final potential. In the second voltametric cycle, the intensity of the band at 1570 nm decreases and increases around -0.3 V pointing to the reversible reduction/re-oxidation of the dimer radical anion accumulated in the layer.

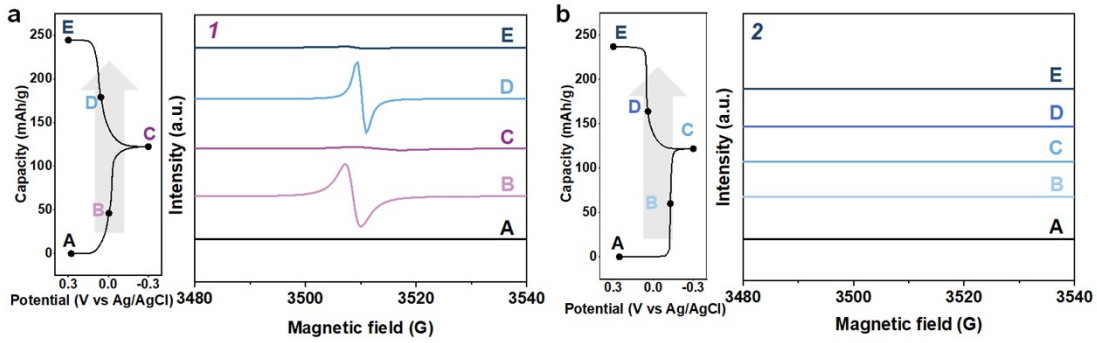

Figure S29 *Ex-situ* EPR tests of **1** (a) and **2 (**b).

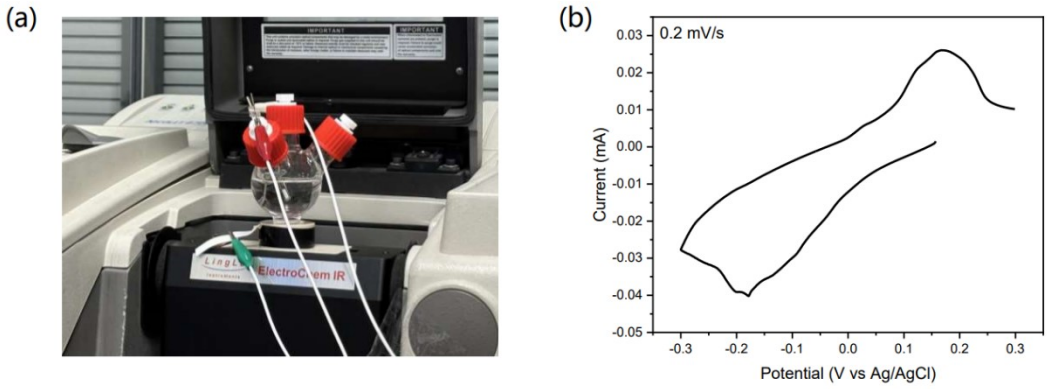

Figure S30 (a) Three-electrode cell for *in-situ* FTIR test. (b) the CV curve of *in-situ* FTIR test.

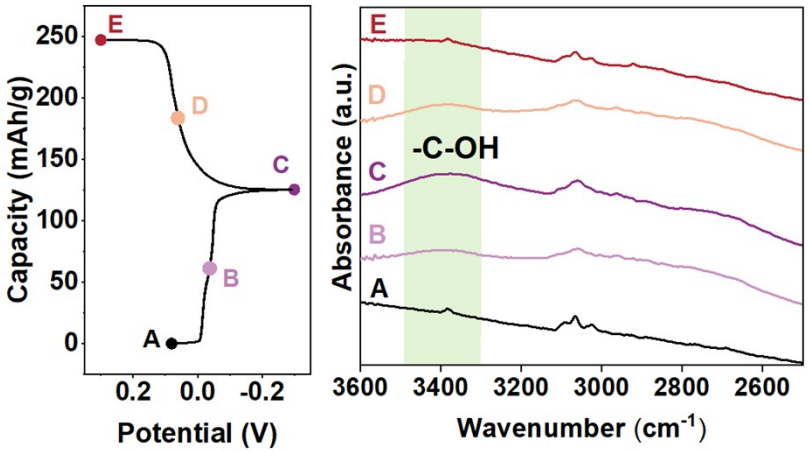

Figure S31 *Ex-situ* FTIR spectrum at the marked points in the discharge-charge curve of **1** electrode at 0.1 A/g.

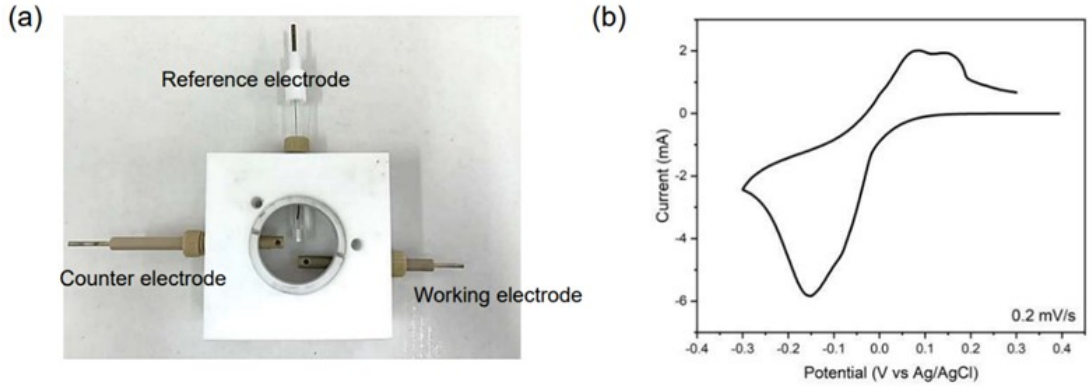

Figure S32 (a) Three-electrode cell for in-situ Raman test. (b) the CV curve of in-situ Raman test.

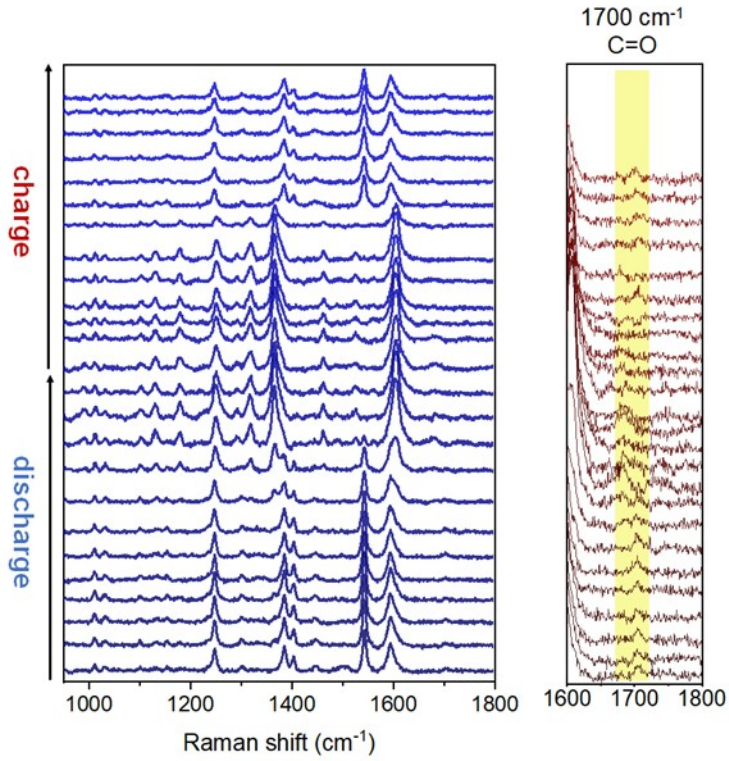

Figure S33 *In-situ* Raman test of **1** electrode.

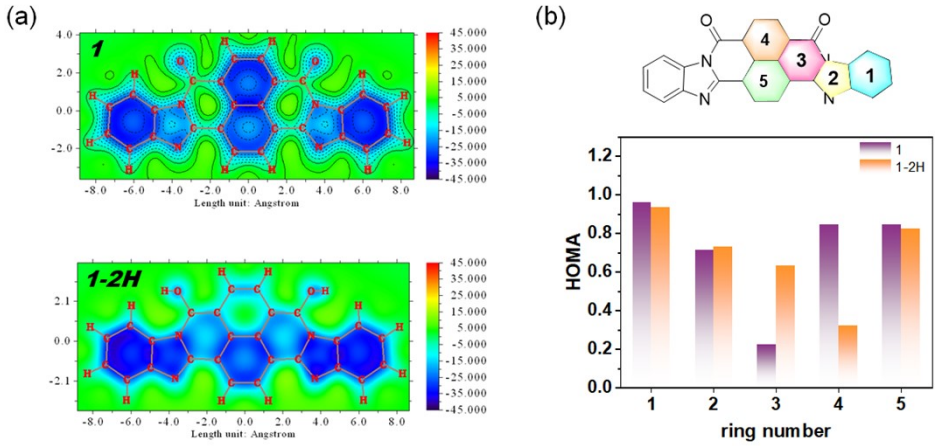

Figure S34 (a) NICS_zz analysis for **1** and protonated molecule **1-2H**. (b) HOMA calculations for **1** and protonated molecule **1-2H** (the closer the HOMA value is to 1, the better the aromaticity).

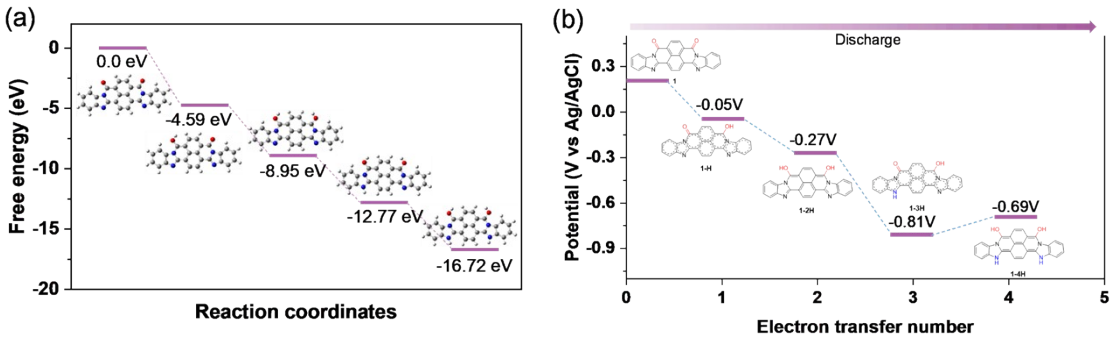

Figure S35 Calculated Gibbs free energy diagrams (a) and potential (b) of **1** during stepped H^+ coordination.

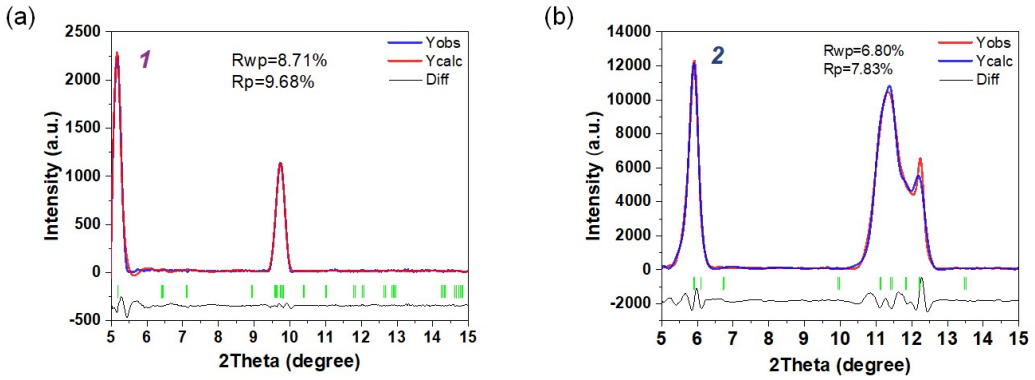

Figure S36 Comparison of the experimental XRD pattern of the discharged perinone isomers with the pattern simulated from the DFT optimized model: (a) *cis*-isomer **1**; (b) *trans*-isomer **2**.

Table S4 Crystallographic Parameters for protonated **1** and **2**.

Compd.	protonated **1**	protonated **2**
formula	$C_{104}H_{72}N_{16}O_{16}$	$C_{52}H_{52}N_8O_{16}$
M_w	1801.81	1045.03
crystal system	triclinic	triclinic
space group	P -1 (2)	P 1 (1)
a [Å]	5.1994	15.5680
b [Å]	18.5313	5.1160
c [Å]	28.2804	16.0729
α [°]	103.5513	89.9958
β [°]	90	68.2058
γ [°]	90	90.0039
V [Å^3]	2649	1188.64
ρ_{calcd} [g cm^{-3}]	1.1294	1.4598

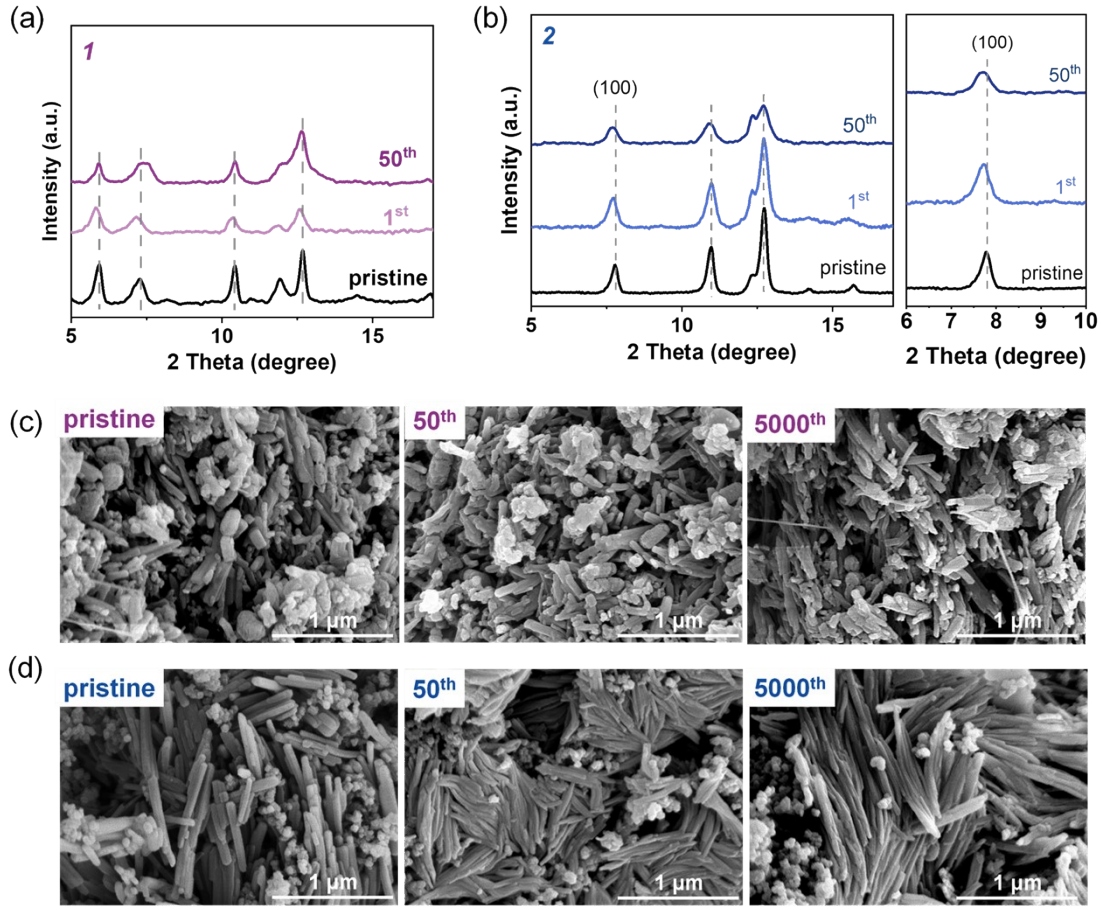

Figure S37 (a) XRD spectrum for **1** electrode of pristine, 1st, and 50th cycles; (b) XRD spectrum for **2** electrode of pristine, 1st, and 50th cycles; (c) SEM images for **1** electrode of pristine, 50th and 5000th cycles; (d) SEM images for **2** electrode of pristine, 50th and 5000th cycles.

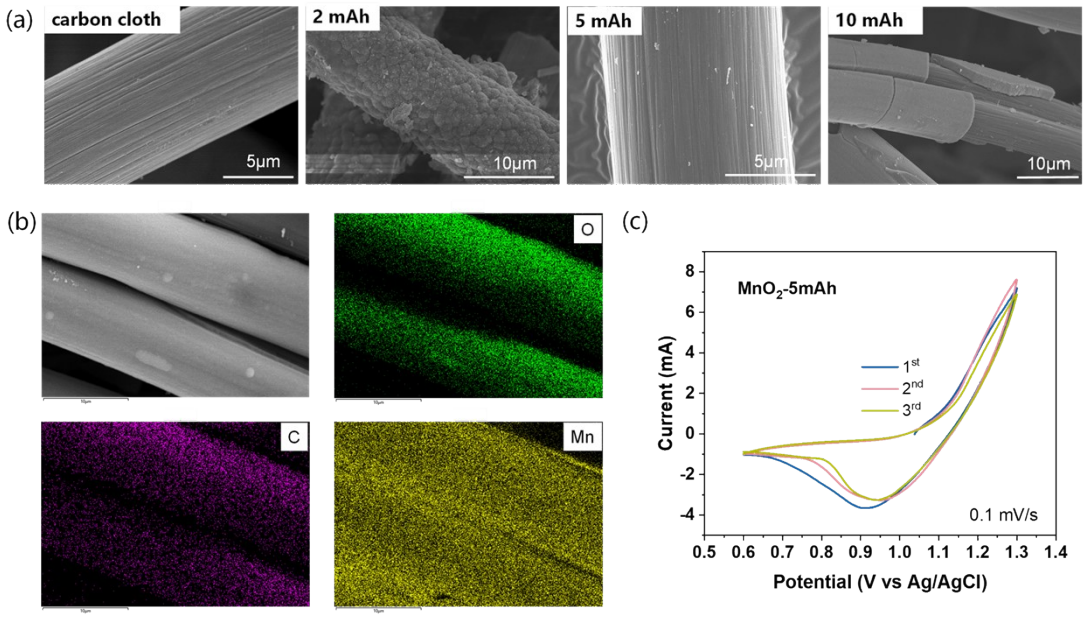

Figure S38 (a) Morphology investigations by SEM images of MnO_2@GF cathode undergoing various MnO_2 electrodeposition capacities on GF. GF electrodes were charged for 2 h, 5 h, and 10 h respectively, at a constant current density of 1 mA. (b) SEM images and EDS-elemental mapping images of MnO_2@GF electrode (pre-deposited 5 mAh); (c) CV curves of MnO_2@GF electrode (pre-deposited 5 mAh).

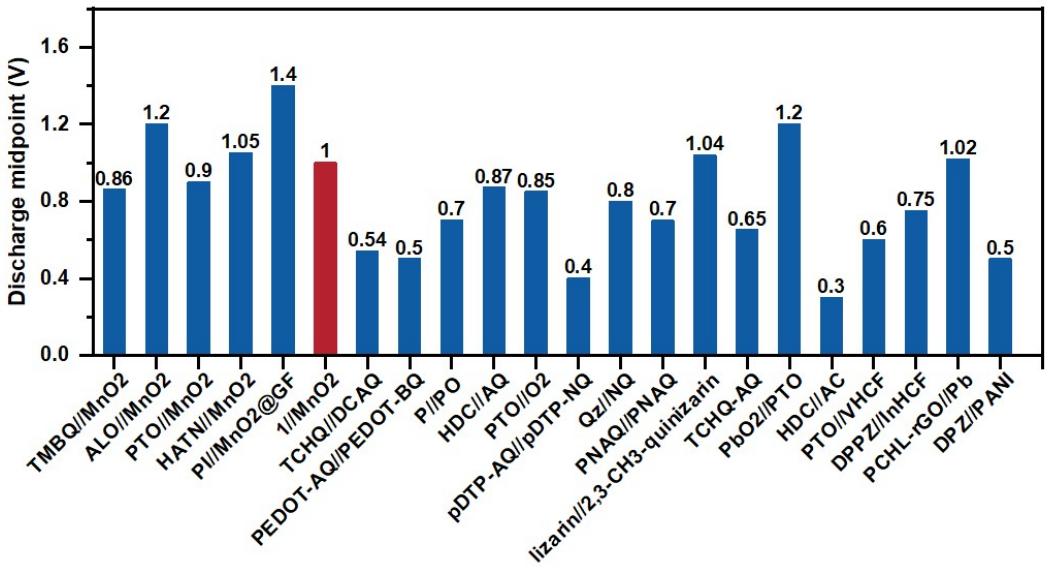

Figure S39 Discharge midpoint comparison of the MnO_2@CC//**1** with other aqueous proton battery based on organic electrode materials. [3-24]

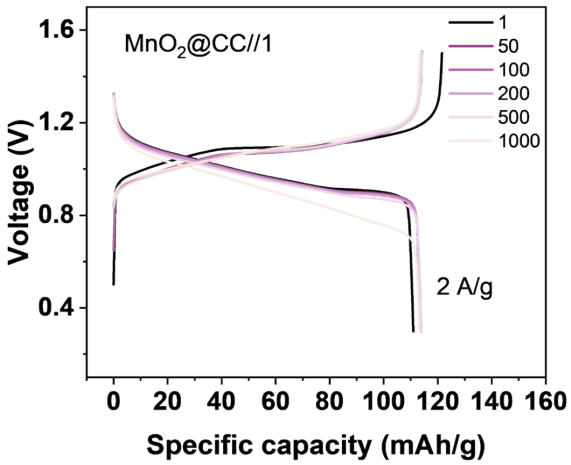

Figure S40 Charge–discharge curves of MnO_2@CC//**1** during long-term cycling at 2 A/g.

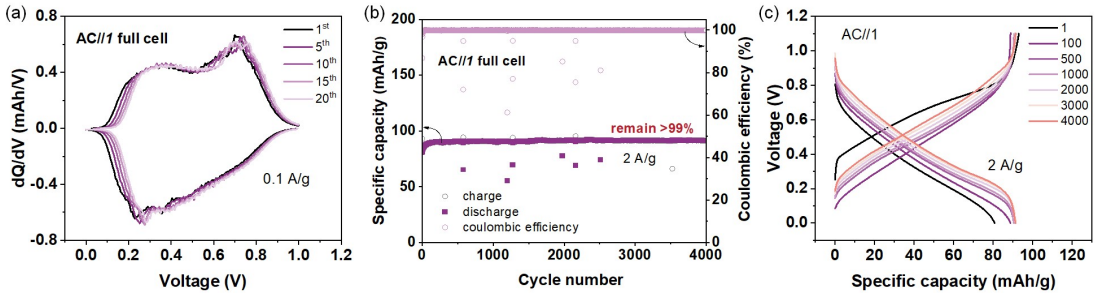

Figure S41 Electrochemical performance of AC//**1** full cell (a) The dQ/dV curve at 0.1 A/g. (b) Cycling stability at 2 A/g. (c) Charge-discharge curves during long-term cycling at 2 A/g.

References

[1] M. Frisch, G. Trucks, H. Schlegel, G. Scuseria, M. Robb, J. Cheeseman, G. Scalmani, V. Barone, G. Petersson, H. Nakatsuji, Gaussian 16, Revision A. 03, Gaussian, Inc.: Wallingford CT, **2016**.

[2] Tian Lu, Feiwu Chen, *J. Comput. Chem.*, **2012**, 33, 580-592.

[3] Z. Guo, J. Huang, X. Dong, Y. Xia, L. Yan, Z. Wang, Y. Wang. *Nat. Commun.* **2020**, 11, 959.

[4] X. Wang, C. Bommier, Z. Jian, Z. Li, R. S. Chandrabose, I. A, et, al. *Angew. Chem. Int. Ed.* **2017**, 56, 2909-2913.

[5] Z. Tie, Y. Zhang, J. Zhu, S. Bi, Z. Niu. *J. Am. Chem. Soc.* **2022**, 144, 10301−10308.

[6] Z. Tie, S. Deng, H. Cao, M. Yao, Z. Niu, J. Chen. *Angew. Chem. Int. Ed.* **2022**, 61, e202115180.

[7] Y. Ma, Y. Wei, W. Han, Y. Tong, A. Song, J. Zhang, H. Li, X. Li, J. Yang. *Angew. Chem. Int. Ed.* **2023**, 62, e202314259.

[8] W. Han, M. Li, Y. Ma, J. Yang. *Electrochim. Acta*, **2022**, 403, 139550.

[9] G. Zhao, X. Yan, Y. Dai, J. Xiong, Q. Zhao, et, al. *Small*, **2023**, 20, 2306071.
[10] X. Wang, J. Zhou, W. Tang, Energy Storage Materials, **2021**, 36, 1-9.
[11] K. C. S. Lakshmi, B. Vedhanarayanan, H.-Y. Cheng, X. B. Ji, H.-H. Shen, T.-W. Lin, *J. Colloid Interface Sci.* **2022**, *619*, 123-131.
[12] T. Sun, H. Du, S. Zheng, J. Shi, X. Yuan, L. Li, Z. Tao, *Small Methods* **2021**, *5*, 2100367.
[13] M. Zhu, L. Zhao, Q. Ran, Y. Zhang, R. Peng, G. Lu, X. Jia, D. Chao, C. Wang, *Adv. Sci.* **2022**, *9*, 2103896.
[14] X. Yang, Y. Ni, Y. Lu, Q. Zhang, J. Hou, G. Yang, X. Liu, W. Xie, Z. Yan, Q. Zhao, J. Chen, *Angew. Chem.* **2022**, *61*, e202209642.
[15] T. Sun, H. Du, S. Zheng, J. Shi, Z. Tao. *Adv. Funct. Mater.* **2021**, *31*, 2010127.
[16] T. Tomai, S. Mitani, D. Komatsu, Y. Kawaguchi, I. Honma. *Sci Rep.* **2014**, *4*, 3591.
[17] R. Emanuelsson, M. Sterby, M. Strømme, M. Sjödin. *J. Am. Chem. Soc.* **2017**, *139*, 4828-4834.
[18] D. Shen, A. M. Rao, J. Zhou, B. Lu, *Angew. Chem.* **2022**, *61*, e202201972.
[19] H. Wang, R. Emanuelsson, C. Karlsson, P. Jannasch, M. Strømme, M. Sjödin. *ACS Appl. Mater. Interfaces* **2021**, *13*, 19099-19108.
[20] L. Tong, Y. Jing, R. Gordon, M. Aziz. *ACS Appl. Energy Mater.* **2019**, *2*, 4016-4021.
[21] Z. Sun, J. Tang, J. Chen, H. Guo, S. Wu, S. Yin, T. Zhao, C. Jia, Q. Meyer, A. Rawal, J. Ho, Y. Fang, C. Zhao, *Small Struct.* **2023**, *4*, 2200257.
[22] J. Qiao, M. Qin, Y. Shen, J. Cao, Z. Chen, J. Xu, *Chem. Commun.* **2021**, *57*, 4307-4310.
[23] M. Shi, J. He, Y. Zhao, L. Zhao, K. Dai, C. Yan, Materials & Design, **2022**, *222*, 111043.
[24] F. Yue, Z. Tie, S. Deng, S. Wang, M. Yang, Z. Niu, *Angew. Chem.* **2021**, *60*, 13882-13886